# JCTC Journal of Chemical Theory and Computation

## Charge and Spin Currents in Open-Shell Molecules: A Unified Description of NMR and EPR Observables

Alessandro Soncini*

*Department of Chemistry, Laboratory of Quantum Chemistry, Katholieke Universiteit Leuven, Celestijnenlaan 200F, B-3001 Heverlee, Belgium*

**Abstract:** The theory of EPR hyperfine coupling tensors and NMR nuclear magnetic shielding tensors of open-shell molecules in the limit of vanishing spin−orbit coupling (e.g., for organic radicals) is analyzed in terms of spin and charge current density vector fields. The ab initio calculation of the spin and charge current density response has been implemented at the Restricted Open-Shell Hartree−Fock, Unrestricted Hartree−Fock, and unrestricted GGA-DFT level of theory. On the basis of this formalism, we introduce the definition of nuclear hyperfine coupling density, a scalar function of position providing a partition of the EPR observable over the molecular domain. Ab initio maps of spin and charge current density and hyperfine coupling density for small radicals are presented and discussed in order to illustrate the interpretative advantages of the newly introduced approach. Recent NMR experiments providing evidence for the existence of diatropic ring currents in the open-shell singlet pancake-bonded dimer of the neutral phenalenyl radical are directly assessed via the visualization of the induced current density.

## 1. Introduction

Open-shell molecules are basic components of chemical and biological systems.[1] They are at the heart of many processes, ranging from simple organic reactions[1] up to more complex chemical processes involving enzymes or nucleic acids.[2] Owing to the extremely short-lived nature of these species, magnetic spectroscopies, such as Electron Paramagnetic Resonance (EPR) and Nuclear Magnetic Resonance (NMR), are primary tools for elucidating their structure.[3,4] Whereas the theoretical and computational investigation of magnetic response properties of open-shell molecules has always played a fundamental role in the interpretation of EPR spectra,[5−10] the theory and computation of molecular properties related to the NMR spectroscopy of paramagnetic species has received comparatively much less attention, although progress in computational capabilities and successful investigations of paramagnetic NMR of coordination compounds and metalloproteins have given new impetus to research in this area.[4,11−14]

Among the theoretical strategies that have been devised and applied to unravel the rich phenomenology underlying magnetic spectroscopies, the representation and analysis of magnetic properties of closed-shell molecules via the induced quantum mechanical current density has been pursued since the early days of NMR spectroscopy.[15−17] In fact, direct visualization of the induced current density has been shown to embody several interpretative advantages. For instance, this approach has introduced very successful concepts in chemistry, such as the ring current model[15−18] explaining anomalous proton chemical shifts of aromatic and antiaromatic molecules, and a definition of chemical aromaticity and antiaromaticity based on the magnetic criterion.[19−25]

An analogous approach to the study of NMR or EPR spectra of open-shell molecules has always been discussed mostly on a theoretical basis. Theoretical predictions concerning the existence and the (diatropic) sense of circulation of the induced current density $\mathbf{J}^{(1)}$ in putative [4*n*] aromatic triplets have been proposed by Fowler et al.,[23] on the basis of the ipsocentric model[24,25] for the analysis of ring currents in $\pi$-conjugated networks. The zeroth-order spin-current $\mathbf{J}^{(0)}$

* Corresponding author e-mail: Alessandro.Soncini@ chem.kuleuven.be.

associated with the ground state of an open-shell system has been considered as a formal starting point to deduce the expression for effective hyperfine spin Hamiltonians in the nonrelativistic limit (see ref 26, Chapter 17, pp 690−692) although no explicit formulation of the property itself (i.e., the tensor components of the hyperfine coupling defined as energy derivatives) in terms of $\mathbf{J}^{(0)}$ has been discussed. A formulation of the EPR $g$ tensor up to second order (i.e., the leading contribution for systems whose ground state is orbitally nondegenerate) in terms of the first order induced current density $\mathbf{J}^{(1)}$ has been introduced in ref 27 (see Chapter 11, pp 398−402). This definition, based on second-order perturbation theory, has been extended to the spin-other-orbit contribution to the $g$ tensor,[28−30] and a computational recipe for its evaluation using London orbitals to accelerate the convergence toward origin-independent results within the spin-polarized Kohn−Sham (KS) DFT formalism has been provided and implemented.[30] Despite these preliminary efforts, to date, to the best of our knowledge, current densities in open-shell systems have always been used at best as computational byproducts of the calculation of second-order response properties, and no attempt has been made to *visualize* and *rationalize* the magnetic response of open-shell systems in terms of current density vector fields.

It is the purpose of this work to introduce the theoretical and computational framework aimed at the representation of the magnetic properties of open-shell molecules in terms of current density vector fields and show how this theoretical approach can be of great use in providing a unified interpretative model for the rationalization of EPR and NMR parameters. One of the basic features that diversifies the response of a closed-shell from that of an open-shell system consists of the presence of the zeroth-order spin current density $\mathbf{J}^{(0)}$ in the latter.[26] In the limit of very low temperatures, this zeroth-order contribution is independent of the strength of the applied magnetic field, which merely provides the direction of a preferred quantization axis for the total spin of the molecule. Accordingly, neglecting spin−orbit coupling in this first introductory study (a very plausible approximation for a vast class of open-shell molecules, e.g., organic radicals, triplets, and open-shell singlets), any attempt at the visualization of the magnetic response of an open-shell molecule must be inclusive of two main contributions: a zeroth-order spin current density $\mathbf{J}^{(0)}$ related to the unperturbed wave function[26] and the usual first-order charge current density $\mathbf{J}^{(1)}$, which contains the full information related to the linear magnetic response of the system.[27,18] In order to compute these quantities, we propose here an efficient ab initio computational procedure based on the Restricted Open-Shell Hartree−Fock (ROHF) wave function. The calculation $\mathbf{J}^{(0)}$ and $\mathbf{J}^{(1)}$ has also been implemented at the Unrestricted Hartree−Fock (UHF) level of theory. Finally, once the unperturbed KS $\alpha$ and $\beta$ spin orbitals are obtained from standard DFT calculation packages within unrestricted GGA-DFT approaches, it is possible to obtain $\mathbf{J}^{(0)}$ and $\mathbf{J}^{(1)}$ by means of straightforward sum-over-states expressions, since in GGA-DFT theories the response to a magnetic field is rigorously computed within a so-called uncoupled formalism.[31,32]

The unified description in terms of $\mathbf{J}^{(0)}$ and $\mathbf{J}^{(1)}$ of the magnetization density arising (i) in zero order, from the ground-state electronic spin, and (ii) in first order from the molecular response to an external field allows one to make straightforward use of the Biot-Savart law from classical electrodynamics to reformulate the magnetic response properties of open-shell systems.[15−18,26−30,33−36] In particular, whereas the detailed tensor expression for the temperature-independent contribution to the NMR nuclear magnetic shielding tensor in terms of $\mathbf{J}^{(1)}$ is very well-known (see, e.g., ref 18), we show here that, in the limit of vanishing spin−orbit coupling, (i) the temperature-dependent contribution to the NMR nuclear magnetic shielding of open-shell molecules and (ii) the EPR hyperfine coupling tensor $A^{\mathrm{I}}_{\alpha\beta}$ can both be reformulated in terms of three-dimensional space integrals of a second-rank spin-current density tensor, defined as the formal derivative of $\mathbf{J}^{(0)}$ with respect to the electronic spin component along the direction of the chosen quantization axis, thus providing a rigorous link between the maps of $\mathbf{J}^{(0)}$ and the calculated components of $A^{\mathrm{I}}_{\alpha\beta}$. The current density formulation of the $g$ tensor based on second-order perturbation theory introduced in ref 27 and extended to include the spin-other-orbit contributions in refs 28−30 clearly provides the natural theoretical basis for the extension of the present analysis to include spin−orbit coupling, a formulation which would need to be further generalized beyond second-order perturbation theory in order to properly describe, e.g., systems whose ground state is orbitally degenerate. But this goes beyond the scope of the present work.

Finally, following on from the successful application of shielding density functions and spin−spin coupling density functions to the interpretation of NMR observables in closed-shell molecules,[33−36] we introduce here the theoretical definition of hyperfine coupling density $A^{\mathrm{I}}_{\alpha\beta}(\mathbf{r})$, a set of scalar functions of position that can be easily computed from $\mathbf{J}^{(0)}$ and plotted all over the molecular domain to assess the contribution of each point in space to the integrated $A^{\mathrm{I}}_{\alpha\beta}$. As an application of the newly developed methodology, we present (i) ab initio calculations of $\mathbf{J}^{(0)}$, $\mathbf{J}^{(1)}$, and $A^{\mathrm{I}}_{\alpha\beta}(\mathbf{r})$ for three small radicals, $BH_2$, $CH_2^-$, and $NH_2$, to discuss and interpret the physical origin their NMR and EPR observables, and (ii) ab initio and broken symmetry GGA-DFT calculations of $\mathbf{J}^{(1)}$ for the neutral phenalenyl radical and its pancake-bonded dimer (an open-shell singlet), to interpret recent NMR experiments and NICS computational analysis concerning the magnetic aromaticity of these open-shell molecules.[37]

## 2. Current Density Representation of an Open-Shell Molecule in a Magnetic Field

The ground state of a molecule characterized by a spinless electron density matrix $P(\mathbf{r},\mathbf{r}')$ and a spin density $Q_\gamma(\mathbf{r})$, ($\gamma =$ x, y, z) is associated with a current density distribution $J_\alpha(\mathbf{r})$ given by[27,38,39]

$$J_\alpha(\mathbf{r}) = -\frac{e}{m}\mathscr{R}\,[p_\alpha P(\mathbf{r},\mathbf{r}')]_{\mathbf{r}'=\mathbf{r}} - \frac{e}{m}\,\epsilon_{\alpha\beta\gamma}\,\nabla_\beta Q_\gamma(\mathbf{r}) \quad (1)$$

where $m$ and $-e$ are the mass and charge of the electron, $p_\alpha$ is the electronic linear momentum, $\epsilon_{\alpha\beta\gamma}$ is the Levi-Civita

Charge and Spin Currents in Open-Shell Molecules

*J. Chem. Theory Comput., Vol. 3, No. 6, 2007* **2245**

third rank skew tensor, and the Einstein's convention for summation over repeated Greek indices is in force. Let us consider an open-shell molecule. In the absence of orbital degeneracy the first term on the rhs of (1) describes the response of the system to an external magnetic field. Accordingly, the spinless density matrix can be expanded to first order in the field as $P(\mathbf{r},\mathbf{r}') = P^{(0)}(\mathbf{r},\mathbf{r}') + P^{(1)}(\mathbf{r},\mathbf{r}')$, and an explicit expression for the first term on the rhs of (1) can be provided according to the well-known equations for the first-order induced current density[27,18]

$$J_\alpha^{(1)}(\mathbf{r}) = \frac{e}{mc} A_\alpha(\mathbf{r})P^{(0)}(\mathbf{r}) - \frac{e}{m} \mathscr{R} [p_\alpha P^{(1)}(\mathbf{r},\mathbf{r}')]_{\mathbf{r}'=\mathbf{r}} \quad (2)$$

where $A_\alpha(\mathbf{r})$ is the vector potential associated with the external magnetic field, and $c$ is the speed of light.

Let us now turn to the second term[26,38,39] on the rhs of (1). The ground state of an open-shell molecule with total spin quantum number $S \neq 0$ consists of a $2S+1$ degenerate multiplet. Each state of the degenerate set can be characterized by a spin projection quantum number $M_S$ along an arbitrary quantization axis; accordingly, the density of spin angular momentum $Q_\gamma(\mathbf{r})$ will depend on which state we consider. However, in accordance with the Wigner-Eckart theorem, the spin densities are in fact all the same except for a proportionality constant.[27] It is therefore expedient to introduce a reduced spin density scalar function, $Q(\mathbf{r})$, common to all components of the multiplet, and an effective spin density operator $Q_{\text{op},\gamma}(\mathbf{r})$ proportional to $Q(\mathbf{r})$ that differentiates the various components when averaged over the corresponding states. Thus

$$Q_{\text{op},\gamma}(\mathbf{r}) = \frac{Q_S(\mathbf{r})}{S} \delta_{\gamma z}S_{\text{op},z} = Q(\mathbf{r})\delta_{\gamma z}S_{\text{op},z} \quad (3)$$

where $Q_S(\mathbf{r})$ is the spin density component along the quantization axis $z$ corresponding to the electronic state with highest spin projection $M_S = S$, and $S_{\text{op},z}$ is the total spin projection operator along $z$. If $|SM_S\rangle$ denotes a spin eigenfunction, the following relationships hold

$$\int \langle SM_S|Q_{\text{op},\gamma}(\mathbf{r})|SM_S\rangle d^3r = \int Q_\gamma(\mathbf{r})d^3r = \langle S_{\text{op},\gamma}\rangle = M_S\delta_{\gamma z} \quad (4)$$

where $\delta_{\gamma z}$ is the Kronecker delta. In the absence of a magnetic field, the averaging of (3) over all $2S+1$ degenerate spin components clearly results in $Q_\gamma(\mathbf{r}) = 0$. In a magnetic field, a physical choice for the quantization axis consists of the direction of the field itself, along which the Zeeman interaction induces a nonzero spin density polarization by splitting the degenerate multiplet into its $2S+1$ components.

With the understanding that the reference frame is always chosen so that the quantization axis $\gamma$ coincides with the direction of the magnetic field, from the second term on the rhs of (1) we can immediately define an effective spin-current density diagonal operator $\mathbf{J}^{(0)}$, solely acting on spin variables within a given multiplet, as

$$J_\alpha^{(0)}(\mathbf{r}) = \mathscr{T}_\alpha^{S_\gamma}(\mathbf{r})S_{op,\gamma}, \quad \mathscr{T}_\alpha^{S_\gamma}(\mathbf{r}) = -\frac{e}{m} \epsilon_{\alpha\beta\gamma}\nabla_\beta Q(\mathbf{r}) \quad (5)$$

where we have introduced the second rank zeroth-order spin current density tensor $\mathscr{T}_\alpha^{S_\gamma}(\mathbf{r})$ formally defined as $\mathscr{T}_\alpha^{S_\gamma}(\mathbf{r}) = \partial J_\alpha^{(0)}/\partial S_\gamma$. Note that $\mathbf{J}^{(0)}$, since defined as the curl of the spin density, is identically divergenceless. It immediately follows that the continuity equation is fulfilled independently of the approximation and basis set used to compute the wave function.

## 3. Current Density Formulation of the Nuclear Hyperfine Coupling Tensor and Density of Hyperfine Coupling

Let us consider an open-shell molecule characterized by total spin $S$ and a magnetic nucleus $J$ with spin $I$. The corresponding nuclear hyperfine coupling constant (HCC) measured in EPR can be rationalized in terms of the splitting of the $(2S+1) \times (2I+1)$ degenerate ground state that is induced by the interaction between nuclear and electron spin magnetic moments.[6,26] The underlying electron-nucleus spin−spin coupling mechanism is described in the nonrelativistic limit by the isotropic Fermi contact (FC) and the traceless anisotropic spin dipolar (SD) Hamiltonians.[6,26,27] If the distance between electron $i$ and nucleus $J$ is called $\mathbf{r}_{iJ}$, the FC and SD Hamiltonians are given by[26,27]

$$H_{\text{FC}}^J = \frac{8\pi}{3} \beta_e\beta_N g_e g_J \sum_{i=1}^{n} \delta(\mathbf{r}_{iJ})\boldsymbol{\sigma}_i\cdot\mathbf{I}_J$$

$$H_{\text{SD}}^J = \beta_e\beta_N g_e g_J \sum_{i=1}^{n} \sigma_{i\lambda}r_{iJ}^{-5}(3r_{iJ\lambda}r_{iJ\mu} - r_{iJ}^2\delta_{\lambda\mu})I_{J\mu} \quad (6)$$

where $\beta_e = e\hbar/2mc$ is the Bohr magneton (in cgs emu units), $\beta_N = e\hbar/2m_pc$ is the nuclear magneton with $m_p$ the proton mass, $\delta(\mathbf{r}_{iJ})$ is the Dirac delta function, $\boldsymbol{\sigma}_i$ is a vector whose components are given by the Pauli matrices associated with electron $i$, and $g_e$ and $g_J$ are the isotropic g-factors for the electron and the nucleus $J$, respectively. The first-order change in the energy of the system caused by (6) is completely equivalent to the splitting of the $(2S+1) \times (2I+1)$ degenerate multiplet produced by the following effective spin Hamiltonians (see, e.g., ref 27 p 389)

$$H_{\text{eff}}^{\text{FC}} = h A_{\text{iso}}^J \mathbf{I}_J\cdot\mathbf{S} \equiv W_{\text{iso}}^{\mathbf{I},\mathbf{S}}, \quad H_{\text{eff}}^{\text{SD}} = h I_{J\lambda}A_{\lambda\mu}^J S_\mu \equiv W_{\text{SD}}^{\mathbf{I},\mathbf{S}} \quad (7)$$

where $A_{\text{iso}}^J$ and $A_{\lambda\mu}^J$ are, respectively, the isotropic and dipolar components of the hyperfine coupling tensor. These can be defined in terms of the scalar spin density function (3) as[27] (in Hz):

$$A_{\text{iso}}^J = \frac{8\pi\beta_e\beta_N g_e g}{3h} \int d\mathbf{r}_1\delta(\mathbf{r}_{1J})Q(\mathbf{r}_1) = \frac{8\pi\beta_e\beta_N g_e g}{3h} Q(\mathbf{R}_J) \quad (8)$$

$$A_{\lambda\mu}^J = \frac{\beta_e\beta_N g_e g}{h} \int d\mathbf{r}_1 r_{1J}^{-5}(3r_{1J\lambda}r_{1J\mu} - r_{1J}^2\delta_{\lambda\mu})Q(\mathbf{r}_1) \quad (9)$$

Within the effective spin Hamiltonian formalism, the terms in (7) can now be interpreted as interaction energies between classical magnetic dipole moments associated with the electronic and nuclear spins, with a total interaction energy given by $W^{\mathbf{I},\mathbf{S}} = W_{\text{iso}}^{\mathbf{I},\mathbf{S}} + W_{\text{SD}}^{\mathbf{I},\mathbf{S}}$.

An alternative expression for $W^{\mathbf{I},\mathbf{S}}$ can be formulated within the current density formalism (see, e.g., ref 26). In fact, according to classical electrodynamics, the interaction energy between the spin current density $\mathbf{J}^{(0)}$ and a nuclear magnetic dipole $\mu^J = g_J\beta_N\mathbf{I}_J$ reads as[26,18]

$$W^{\mathbf{I},\mathbf{S}} = -\frac{1}{c}\int d\mathbf{r}\, \mathbf{A}^{\mu_J}\cdot\mathbf{J}^{(0)}(\mathbf{r}) \qquad (10)$$

where the classical vector potential associated with nucleus $J$ is $A_\alpha^{\mu_J}(\mathbf{r}) = g_J\beta_N\epsilon_{\alpha\beta\gamma}I_{J\beta}(r_\gamma - R_{J\gamma})/|\mathbf{r} - \mathbf{R}_J|^3$. Using the definition for $\mathbf{J}^{(0)}$, we can write (10) more explicitly as

$$W^{\mathbf{I},\mathbf{S}} = -\frac{g_J\beta_N}{c}\epsilon_{\alpha\beta\gamma}I_{J\beta}S_\lambda \int \mathscr{F}_\alpha^{S_\lambda}(\mathbf{r})\frac{(r_\gamma - R_{J\gamma})}{|\mathbf{r} - \mathbf{R}_J|^3}\,d\mathbf{r} \quad (11)$$

The consistency between definitions (11) and (7) can be easily checked via the procedure adopted, for instance, in ref 36. Definition (11) was implicit, e.g., in the derivation of the effective spin Hamiltonians (17) via $\mathbf{J}^{(0)}$ given in ref 26, although the present form, via the introduction of the components of a second-rank spin current density tensor (5), delivers an expression that is explicitly bilinear in $\mathbf{I}$ and $\mathbf{S}$, a fact that is well-known to be useful in defining molecular properties in terms of analytic energy derivatives, rather than via finite-field approaches.

Given the fact that (7) provides an exact factorization of the problem into separate space and spin manifolds, it is now possible to provide a formal definition for the HCCs in terms of energy derivatives with respect to the components of the electron spin $\mathbf{S}$ and the nuclear spin $\mathbf{I}_J$, as

$$A_{\lambda\mu}^J = A_{\text{iso}}^J\delta_{\lambda\mu} + A_{\lambda\mu}^J = \frac{1}{h}\frac{\partial^2 W^{\mathbf{I},\mathbf{S}}}{\partial I_{J\lambda}\partial S_\mu} \qquad (12)$$

where $W^{\mathbf{I},\mathbf{S}}$ is given either by the sum of eqs 7 or by eq 11.

Thus, the formal definition (12), which trivially recovers (8) and (9) when used with (7), leads to a new expression for the nuclear hyperfine coupling tensor, when applied to the energy definition based on the current density formalism (11):

$$A_{\lambda\mu}^J = -\frac{g_J\beta_N}{hc}\epsilon_{\lambda\gamma\alpha}\int d\mathbf{r}\,\frac{(r_\gamma - R_{J\gamma})}{|\mathbf{r} - \mathbf{R}_J|^3}\mathscr{F}_\alpha^{S_\mu}(\mathbf{r}) \qquad (13)$$

The advantage of this expression consists of the fact that it provides a formulation of each tensor component describing hyperfine coupling that is formally based on classical electrodynamics and thus puts it on an equal footing with analogous definitions introduced for NMR and EPR observables, such as the nuclear magnetic shielding,[15–18] the indirect nuclear spin–spin coupling tensor,[39,34,36] and the $g$-tensor.[27–30]

As with nuclear magnetic shielding[33,35] and nuclear spin–spin coupling tensors,[34,36] given the current density definition of hyperfine coupling constants (13), it is now straightforward to define a *density of hyperfine coupling* as

$$A_{\lambda\mu}^J(\mathbf{r}) = -\frac{g_J\beta_N}{hc}\epsilon_{\lambda\gamma\alpha}\frac{(r_\gamma - R_{J\gamma})}{|\mathbf{r} - \mathbf{R}_J|^3}\mathscr{F}_\alpha^{S_\mu}(\mathbf{r}) \qquad (14)$$

These scalar functions can easily be plotted over the molecular domain and interpreted as a pointwise partition of the Biot-Savart law, in that they provide a straightforward visualization of the point-by-point contribution from the spin current distribution to the magnetic field induced at the site of nucleus $J$. It is important to stress that in principle the set of scalar functions (14) is not uniquely defined. It is in fact possible to add to (14) an arbitrary scalar function that integrates to zero, and the resulting hyperfine density would exactly lead on integration to the same set of observables. It is however not straightforward to define a physically sensible transformation that would accomplish such a change in (14), also given the fact that the hyperfine density is given by the product of the derivatives of two functions (the spin current and the nuclear vector potential) that are both origin-invariant and, in the case of the current, even gauge invariant. At any event, although endowed with a certain degree of arbitrariness, it will be shown later on that the hyperfine coupling density (14) is indeed very well-defined from a conceptual point of view and useful to interpret spin current density maps.

## 4. Current Density Formulation of the Nuclear Magnetic Shielding Tensor in Paramagnetic Molecules

NMR chemical shifts for open-shell molecules, in the limit of small spin−orbit coupling, can be rationalized in terms of two main contributions.[11,12] The first consists of the usual temperature independent or orbital contribution, also accounting for NMR chemical shifts in closed-shell molecules. The current density formulation of the orbital term for an open-shell molecule can be obtained straightforwardly for any magnetic nucleus $J$ from the analogous definition for the closed-shell case, given by the space integral[18]

$$\sigma_{J,\alpha\beta} = \frac{\partial^2 W^{\mu_J\mathbf{B}}}{\partial\mu_{J\alpha}\partial B_\beta} = -\frac{1}{c}\epsilon_{\alpha\lambda\mu}\int d\mathbf{r}\,\frac{r_\lambda - R_{J\lambda}}{|\mathbf{r} - \mathbf{R}_J|}\mathscr{F}_\mu^{B_\beta}(\mathbf{r}) \qquad (15)$$

where the first-order current density tensor $\mathscr{F}_\gamma^{B_\delta}(\mathbf{r})$ is defined as $\mathscr{F}_\gamma^{B_\delta}(\mathbf{r}) = \partial J_\gamma^{(1)}/\partial B_\delta$. The induced current tensor $\mathscr{F}_\gamma^{B_\delta}(\mathbf{r})$ is routinely calculated and visualized for closed-shell molecules.[18,22,24,25,41] On the other hand, in studies on open-shell molecules $\mathscr{F}_\gamma^{B_\delta}(\mathbf{r})$ has so far appeared just as an intermediate computational byproduct used to recover, on numerical integration over a three-dimensional grid, the value of $g$-tensor components,[28–30] and no attempt at the visualization of $\mathbf{J}^{(1)}$ and interpretation of the integrated magnetic properties based on current density plots appears to exist in the literature.

The second (and dominant) contribution to the observed NMR chemical shift in paramagnetic species is absent in closed-shell molecules, as it arises from the interaction between the electron spin density and the nuclear magnetic moments.[11–14] Let us briefly discuss the origin of this term. The nuclear shielding tensor is defined as a second derivative of the energy with respect to the nuclear dipole and the external field (see eq 15). Accordingly, since the interaction between the spin density distribution and the nuclear magnetic moment (see (7) or (11)) does not formally depend

Charge and Spin Currents in Open-Shell Molecules

*J. Chem. Theory Comput., Vol. 3, No. 6, 2007* **2247**

on the external field, it follows that the contribution from the electron-nucleus spin–spin coupling to the NMR shielding is zero for a pure spin state. However, as highlighted, e.g., in ref 11, owing to the rapid times associated with electron spin relaxation when compared to those involved in the NMR experiment, for high enough thermal energy $k_BT$ (where $T$ is the absolute temperature and $k_B$ the Boltzmann constant) the electron spin density magnetization experienced by the nuclei consists of a thermal average over the field-dependent Zeeman-split spin states. Carrying out the statistical sum within the Van Vleck approximation[12] ($g\beta B \ll k_BT$), one obtains the following expression for the average component of the spin along the quantization axis[11,12]

$$\langle S_\gamma \rangle = - g\beta B_\gamma \frac{S(S+1)}{3k_BT} \quad (16)$$

which introduces a magnetic field dependence in the expression for the thermal average of $W^{I,S}$. Thus, substitution of (16) into (11) leads to a new expression for the temperature-dependent contribution to $\sigma_{I,\alpha\beta}$ in terms of $\mathbf{J}^{(0)}$ as

$$\sigma^{\mathbf{S}}_{I,\alpha\beta} = \frac{\partial^2 \langle W^{I,S} \rangle}{\partial \mu_{I\alpha} \partial B_\beta} = \frac{g\beta S(S+1)}{3k_BTc} \epsilon_{\alpha\lambda\mu} \int d\mathbf{r} \frac{(r_\lambda - R_{I\lambda})}{|\mathbf{r} - \mathbf{R}_I|^3} \mathcal{F}^{S_\beta}_\mu(\mathbf{r}) \quad (17)$$

Equations 13, 15, and 17 share the same three-dimensional integral structure, involving a spin or charge current density distribution, thereby providing a common framework where to describe NMR and EPR observables in terms of maps of spin and charge current density and, accordingly, in terms of concepts based on classical electrodynamics. It is important to stress that these expressions do not define an improved methodology to obtain the numerical value of the response tensor, as they would recover on integration exactly the same results as those obtained via ordinary response theory, provided the same choice of method and basis set is made. Vice versa, the current density tensors appearing in (13), (15), and (17) are not trivial byproducts of normal response calculations, as they involve the explicit buildup of the perturbed and unperturbed wave functions and their spatial gradients over a defined grid of points. The usefulness of expressions like (13), (15), and (17) lies in the fact that they provide an exact connection between the maps of spin and charge current density and the integrated response properties, thus setting a rigorous basis for analyzing and rationalizing the results within classical electromagnetism theory. Next, we describe an ab initio computational procedure to evaluate $\mathbf{J}^{(0)}$ and $\mathbf{J}^{(1)}$ and present a few applications.

## 5. (Coupled)-Hartree–Fock Calculation of Charge and Spin Currents in Open-Shell Molecules

Let the one-row matrix $\chi$ contain a set of atomic basis functions and the matrices $\mathbf{c}_i^{(0)}$ contain on the columns the coefficients for the ROHF doubly occupied ($i = 1$), singly occupied ($i = 2$), and virtual ($i = 3$) molecular orbitals (MOs)

represented in the basis $\chi$. The MO's $\mathbf{c}_i^{(0)}$ are self-consistent solutions to[27]

$$\mathbf{F}_{\text{eff}}^{(0)}\mathbf{R}_i^{(0)} - \mathbf{R}_i^{(0)}\mathbf{F}_{\text{eff}}^{(0)} = \mathbf{0}, \quad i = 1,2$$

$$\mathbf{F}_{\text{eff}}^{(0)} = a\mathbf{R'}_2^{(0)}\mathbf{F}_1^{(0)}\mathbf{R'}_2^{(0)} + b\mathbf{R'}_1^{(0)}\mathbf{F}_2^{(0)}\mathbf{R'}_1^{(0)} + c\mathbf{R'}_3^{(0)}(2\mathbf{F}_1^{(0)} - \mathbf{F}_2^{(0)})\mathbf{R'}_3^{(0)} \quad (18)$$

where $\mathbf{R'}_i^{(0)} = \mathbf{1} - \mathbf{R}_i^{(0)}$, $\mathbf{R}_i^{(0)} = \mathbf{c}_i^{(0)}\mathbf{c}_i^{(0)\dagger}$ ($i = 1,2,3$) are the density matrices represented in the basis $\chi$; $\mathbf{F}_i^{(0)} = \mathbf{h}^{(0)} + \mathbf{G}_i^{(0)}$ are the Fock Hamiltonians for the doubly and singly occupied subspaces ($i = 1,2$) represented on $\chi$ and defined, e.g., in refs 27, 40, 43; and $a$, $b$, and $c$ are arbitrary nonzero convergence parameters. Since in ROHF the spin density is completely described by the singly occupied MO's space, the spin current density tensor defined by eq 5 can be straightforwardly written in terms of $\mathbf{R}_2^{(0)}$ alone as

$$\mathcal{F}^{S_\gamma}_\alpha(\mathbf{r}) = - \frac{e}{m} \epsilon_{\alpha\beta\gamma} \{ \nabla_\beta \chi \mathbf{R}_2^{(0)} \chi^\dagger + \chi \mathbf{R}_2^{(0)} \nabla_\beta \chi^\dagger \} \quad (19)$$

In order to compute $\mathbf{J}^{(1)}$, the ROHF equations (18) are expanded to first order in the magnetic field, resulting in[43]

$$\mathbf{F}_{\text{eff}}^{(0)}\mathbf{R}_i^{(1)} - \mathbf{R}_i^{(1)}\mathbf{F}_{\text{eff}}^{(0)} + \mathbf{F}_{\text{eff}}^{(1)}\mathbf{R}_i^{(0)} - \mathbf{R}_i^{(0)}\mathbf{F}_{\text{eff}}^{(1)} = \mathbf{0}, \quad i = 1,2 \quad (20)$$

which defines the Coupled-ROHF (CROHF) procedure. It can be shown, using the projector properties of the unperturbed density matrices,[43] that the first-order densities can be written as

$$\mathbf{R}_1^{(1)} = (\mathbf{x}_1 + \mathbf{x}_1^\dagger) + (\mathbf{x}_0 + \mathbf{x}_0^\dagger)$$

$$\mathbf{R}_2^{(1)} = (\mathbf{x}_2 + \mathbf{x}_2^\dagger) - (\mathbf{x}_0 + \mathbf{x}_0^\dagger) \quad (21)$$

with $\mathbf{x}_0 = \mathbf{R}_1^{(0)} \mathbf{R}_1^{(1)} \mathbf{R}_2^{(0)}$, $\mathbf{x}_1 = \mathbf{R}_1^{(0)} \mathbf{R}_1^{(1)} \mathbf{R}_3^{(0)}$, and $\mathbf{x}_2 = \mathbf{R}_2^{(0)} \mathbf{R}_2^{(1)} \mathbf{R}_3^{(0)}$. A method for the iterative solution of (20), based on three separate iterative procedures for the calculation of $\mathbf{x}_0$, $\mathbf{x}_1$, and $\mathbf{x}_2$, was described in ref 43.

Here we propose an alternative computational strategy, based on the direct evaluation of the perturbed MO's coefficients for the doubly and singly occupied subspaces. Let us define $\phi_j^{(1)}(\mathbf{r}) = \chi \mathbf{d}_j^{(1)}$ and $\phi_k^{(1)}(\mathbf{r}) = \chi \mathbf{s}_k^{(1)}$, with $j$ ($k$) denoting a doubly (singly) occupied MO. It can easily be shown that equations (21) can be recast as

$$\mathbf{R}_1^{(1)} = \sum_j^{\text{doubly-occ}} (\mathbf{c}_j^{(0)}\mathbf{d}_j^{(1)\dagger} + \mathbf{d}_j^{(1)}\mathbf{c}_j^{(0)\dagger})$$

$$\mathbf{R}_2^{(1)} = \sum_k^{\text{singly-occ}} (\mathbf{c}_k^{(0)}\mathbf{s}_k^{(1)\dagger} + \mathbf{s}_k^{(1)}\mathbf{c}_k^{(0)\dagger}) \quad (22)$$

Accordingly, (20) can now be solved by setting up a single iterative procedure for the unknown perturbed coefficient matrices $\mathbf{d}_j^{(1)}$ and $\mathbf{s}_k^{(1)}$, by defining the Hartree–Fock propagators for the doubly and singly occupied subspaces as

$$\mathbf{M}_1^j = \sum_k^{\text{singly-occ}} \frac{\mathbf{c}_k^{(0)}\mathbf{c}_k^{(0)\dagger}}{\epsilon_j - \epsilon_j} + \sum_m^{\text{vir}} \frac{\mathbf{c}_m^{(0)}\mathbf{c}_m^{(0)\dagger}}{\epsilon_j - \epsilon_m}, \quad j \in \text{doubly-occ}$$

$$\mathbf{M}_2^k = \sum_j^{\text{doubly-occ}} \frac{\mathbf{c}_j^{(0)}\mathbf{c}_j^{(0)\dagger}}{\epsilon_k - \epsilon_i} + \sum_m^{\text{vir}} \frac{\mathbf{c}_m^{(0)}\mathbf{c}_m^{(0)\dagger}}{\epsilon_k - \epsilon_m}, \quad k \in \text{singly-occ}$$

$$(23)$$

and iteratively propagating the unperturbed MOs according to

$$\mathbf{d}_j^{(1)} = \mathbf{M}_1^j \mathbf{F}_{\text{eff}}^{(1)}\mathbf{c}_j^{(0)}, \quad \mathbf{s}_k^{(1)} = \mathbf{M}_2^k \mathbf{F}_{\text{eff}}^{(1)}\mathbf{c}_k^{(0)} \qquad (24)$$

From the converged value of $\mathbf{d}_j^{B_\beta}$ and $\mathbf{s}_k^{B_b}$ (the superscript $B_\beta$ labels the components of the perturbing magnetic dipole operator) the CROHF induced current density (2) can finally be computed as

$$\mathscr{P}_\alpha^{B_\beta}(\mathbf{r}) = -\frac{e}{2mc}\epsilon_{\alpha\beta\gamma}r_\gamma\chi\mathbf{D}\chi^\dagger +$$
$$\frac{4ie\hbar}{m}\sum_j^{\text{doubly-occ}}\{\mathbf{d}_j^{B_\beta\dagger}\chi^\dagger\nabla_\alpha\chi\mathbf{c}_j^{(0)} - \mathbf{c}_j^{(0)\dagger}\chi^\dagger\nabla_\alpha\chi\mathbf{d}_j^{B_\beta}\} +$$
$$\frac{2ie\hbar}{m}\sum_k^{\text{singly-occ}}\{\mathbf{s}_k^{B_\beta\dagger}\chi^\dagger\nabla_\alpha\chi\mathbf{c}_k^{(0)} - \mathbf{c}_k^{(0)\dagger}\chi^\dagger\nabla_\alpha\chi\,\mathbf{s}_k^{B_\beta}\} \quad (25)$$

where $\mathbf{D} = 2\mathbf{R}_1 + \mathbf{R}_2$. The routines for the CROHF evaluation of magnetic response have been implemented in the SYSMO package.[42]

A procedure for (i) the Coupled-UHF (CUHF) magnetic response calculation and (ii) the Unrestricted-GGA-DFT (UDFT) magnetic response calculation based on zeroth-order KS spin-orbitals obtained from the program Gaussian 03[44] has also been implemented. The CUHF and UDFT computational schemes will not be described here, as they have been implemented following well-known procedures.[30] The CROHF, CUHF, and UDFT schemes for the calculation of the first-order current (25) have been implemented within the four distributed-origin approaches generally known as Continuous distribution of The Origin of the Current Density (CTOCD)-methods.[45-47] These methods have been shown to converge to origin-independent results for the magnetic response with relatively small basis sets.[47] Also, for closed-shell molecules, it has been shown that the DZ or *ipsocentric* variant of the CTOCD methods allows an optimal orbital partition of the induced current density, thus providing a frontier orbital model for the rationalization of the magnetic response of $\pi$-conjugated systems.[24,25] The question of open-shell aromaticity[48,49] and its relation with the induced current density[23] can now be quantitatively assessed via plots of (25) or similar expressions corresponding to the CTOCD methods.

## 6. Results and Discussion

As preliminary applications of the developed methodology, first we report here the calculation of the zero- and first-order current density and of the density of hyperfine coupling in the open-shell molecules $BH_2$, $CH_2^-$, and $NH_2$. Next, as further applications of the newly developed methodology, we present the calculation of maps of induced current density $\mathbf{J}^{(1)}$ for (i) the neutral phenalenyl radical and (ii) the pancake-

**Table 1.** Hyperfine Coupling Constant Tensor Components Relative to the Heavy Atoms B, C, and N, Resulting from Numerical Integration of $\mathbf{J}^{(0)}$ for the Three Molecules $BH_2$, $CH_2^-$, and $NH_2{}^a$

| $BH_2$ | $A_{\text{iso}}$ | $A_{C2}$ | $A_{\parallel}$ | $A_\perp$ |
|---|---|---|---|---|
| ROHF | 324.1 | 78.4 | −39.5 | −38.9 |
| UHF | 365.2 | 80.4 | −38.9 | −41.4 |
| RAS-II[b] | 323.3 | 79.7 | −38.8 | −40.9 |

| $CH_2$ | $A_{\text{iso}}$ | $A_{C2}$ | $A_{\parallel}$ | $A_\perp$ |
|---|---|---|---|---|
| ROHF | | −58.3 | −58.1 | 116.4 |
| UHF | 135.5 | −56.4 | −62.7 | 119.1 |
| RAS-II[b] | 59.5 | −56.0 | −59.3 | 115.3 |

| $NH_2$ | $A_{\text{iso}}$ | $A_{C2}$ | $A_{\parallel}$ | $A_\perp$ |
|---|---|---|---|---|
| ROHF | | −42.3 | −42.2 | 84.5 |
| UHF | 42.5 | −43.0 | −41.2 | 84.2 |
| RAS-II[b] | 26.6 | −41.6 | −40.9 | 82.5 |

$^a$ All results are in MHz. $^b$ From calculations reported in ref 11.

bonded dimer of the neutral phenalenyl radical. This study stems from the recent discussion of $^1H$ NMR experimental data and NICS calculations performed on the dimer compound, in which the measured proton chemical shifts have been interpreted in terms of the existence of a deshielding *ring current* in the dimer singlet diradical, a molecule that NICS calculations confirm as an open-shell aromatic $\pi$-complex.[37]

**6.1. Current Density Maps for Small Radicals.** The experimental geometries reported in ref 11 have been employed in the present calculations. The three $C_{2v}$ molecules have $S = 1/2$ ground states with symmetries $^2A_1$ ($BH_2$), $^2B_1$ ($CH_2^-$), and $^2B_1$ ($NH_2$). All the calculations were performed at the (Coupled) ROHF and UHF level of theory using the aug-cc-pVTZ basis set. The spin and charge current densities have been computed and integrated over the whole molecular domain using (i) eq 13 to obtain the isotropic and dipolar components of the HCC for the B, C, and N nuclei (see Table 1) and (ii) eq 15 to obtain the orbital (temperature independent) contribution to the paramagnetic shielding tensor components for B, C, and N (see Table 2). In the same tables we also report more accurate calculations performed at the RAS-II level of theory, taken from ref 11, for the sake of comparison. The results in Table 1 show that the uncorrelated ROHF and UHF approaches perform quite well for these simple systems. It can be seen that the uncorrelated calculations reproduce at a quantitative level the RAS-II dipolar components of $A^1_\alpha\beta$ for all three molecules and $A_{\text{iso}}$ for the $BH_2$. However, the isotropic part of the hyperfine coupling for $CH_2^-$ and $NH_2$ shows only qualitative agreement with the more accurate RAS-II results. The HCCs for $CH_2^-$ and $NH_2$ were calculated at the UHF level of theory in order to account for the spin density polarization at the site of the heavy nucleus. This effect cannot be recovered within the ROHF approach, because of the nodal character at the nuclear site of the $p$ atomic orbital hosting the unpaired electron density and the absence of spin polarization effects within this approach. Accordingly, the overestimation of spin density at the C and N nuclei can be reasonably ascribed to higher-spin contamination of the UHF wave function. Since

Charge and Spin Currents in Open-Shell Molecules

*J. Chem. Theory Comput., Vol. 3, No. 6, 2007* **2249**

***Table 2.*** Paramagnetic Nuclear Magnetic Shielding Tensor Components (Orbital Contribution Only) Relative to the Heavy Atoms B, C, and N, Resulting from Numerical Integration of $\mathbf{J}^{(1)}$ Computed Both Using a Common Origin (CO) and Using the Distributed Origin Method CTOCD-PZ2 (PZ2) for the Three Molecules $BH_2$, $CH_2^-$, and $NH_2$, Using an aug-cc-pVTZ Basis Set[a]

| $BH_2$ | $\sigma_{iso}$ | $\sigma_{C2}$ | $\sigma_{\parallel}$ | $\sigma_{\perp}$ |
|---|---|---|---|---|
| CROHF−CO | −107.5 | −17.9 | −409.7 | 105.3 |
| CROHF-PZ2 | −115.5 | −22.8 | −426.5 | 102.7 |
| CUHF−CO | −85.1 | −18.5 | −343.0 | 106.2 |
| CUHF-PZ2 | −92.8 | −23.4 | −358.6 | 103.6 |
| RAS-II[b] | −167.6 | −29.3 | −569.5 | 95.9 |

| $CH_2^-$ | $\sigma_{iso}$ | $\sigma_{C2}$ | $\sigma_{\parallel}$ | $\sigma_{\perp}$ |
|---|---|---|---|---|
| CROHF−CO | 7.8 | 74.7 | −273.5 | 222.1 |
| CROHF-PZ2 | 5.1 | 72.8 | −279.3 | 221.6 |
| UHF−CO | 30.3 | 83.4 | −216.4 | 223.8 |
| UHF-PZ2 | 27.8 | 81.6 | −221.5 | 223.3 |
| RAS-II[b] | −19.4 | 58.3 | −350.7 | 233.8 |

| $NH_2$ | $\sigma_{iso}$ | $\sigma_{C2}$ | $\sigma_{\parallel}$ | $\sigma_{\perp}$ |
|---|---|---|---|---|
| ROHF−CO | −237.6 | −78.9 | −891.9 | 257.9 |
| ROHF-PZ2 | −241.3 | −81.4 | −899.7 | 257.3 |
| UHF−CO | −184.2 | −54.6 | −756.0 | 258.1 |
| UHF-PZ2 | −187.5 | −57.0 | −763.0 | 257.5 |
| RAS-II[b] | −291.1 | −109.6 | −1029.6 | 265.9 |

[a] All results are in ppm. [b] From calculations reported in ref 11.

in this introductory study the focus is on a novel method providing a pictorial representation of physical mechanisms, rather than on numerical accuracy, we did not implement procedures to project out higher spin components from the UHF wave function. However, it is clear that the qualitative agreement of the results for $A_{iso}$ and the quantitative agreement of the calculated values for the anisotropic components of $A^1{}_{\alpha\beta}$ represent a sufficiently reliable framework whereon to base a sound analysis of the corresponding spin current density functions.

The results for the orbital part of the paramagnetic shielding tensors computed at the CROHF and CUHF level of theory within the current density formalism are reported in Table 2. They display overall good agreement with the RAS-II results. As for the closed-shell case, the computation of these quantities within the finite basis set approach can suffer from gauge-origin dependence. We explored this possibility by computing $\mathbf{J}^{(1)}$ both within the common origin (CO) approximation and within the distributed origin approach CTOCD in its PZ2 variant, which performs the best among the CTOCD schemes.[47] As it is evident from the results reported in Table 2, the agreement between CO and PZ2 is reasonably good, showing that for these simple molecules the aug-cc-pVTZ basis set already leads to results that do not display significant gauge-origin dependence. The best noncorrelated method appears to be CROHF-PZ2. The worst performance when CROHF and CUHF results are compared with RAS-II is observed for $CH_2^-$. Although the sign and relative magnitudes of the individual tensor components computed at the CROHF level are in qualitative
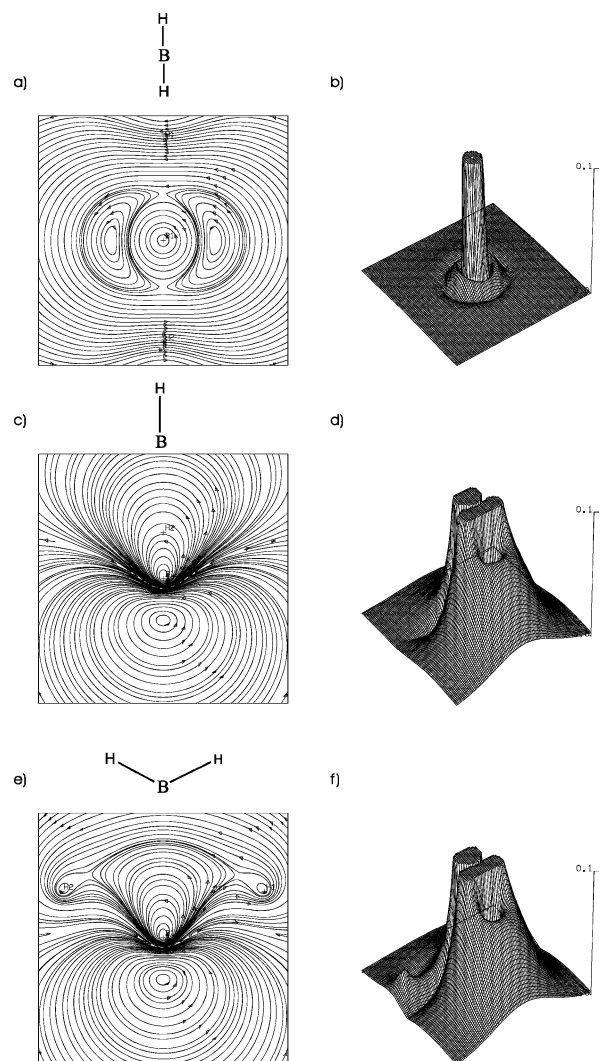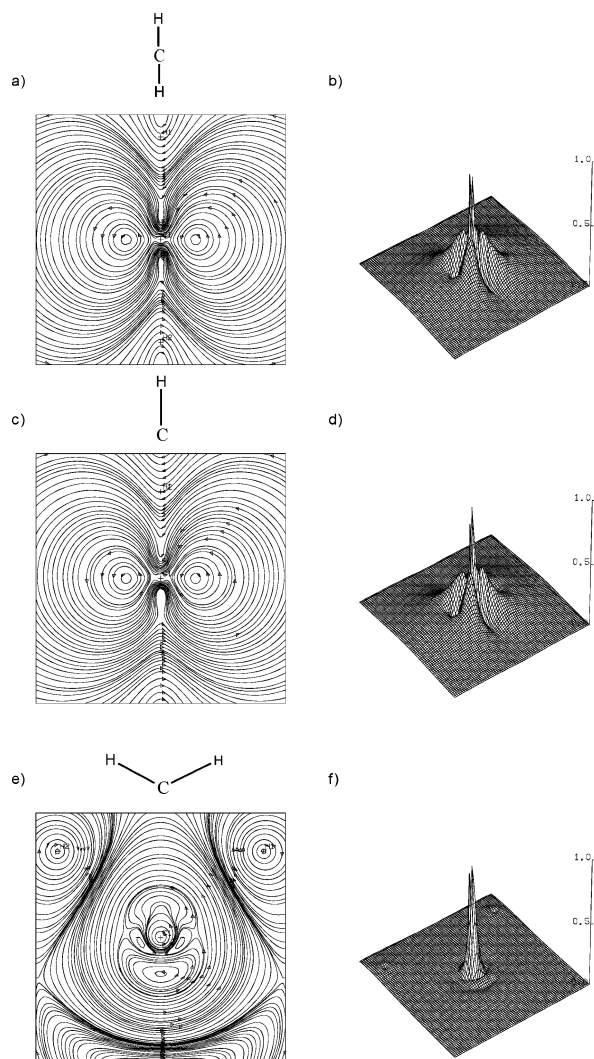


**Figure 1.** Streamlines (left column) and modulus (right column) of the ROHF spin-current density $\mathbf{J}^{(0)}$ characterizing the magnetic field-split ground-state doublet of BH2, plotted for three different orientations of the field (quantization axis): (a) and (b) field along the $C_2$ axis; (c) and (d) field in the molecular plane and perpendicular to the $C_2$ axis; and (e) and (f) field perpendicular to the molecular plane. All maps are plotted over a plane containing the boron atom.

agreement with the RAS-II results, the average shielding has a different sign from that computed at the RAS-II level.

However, even within the RAS-II approximation, the isotropic shielding is relatively small, and the main reason for this is the cancellation between the strong paramagnetic component along the direction perpendicular to the $C_2$ axis and contained in the molecular plane ($\sigma_{\parallel}$) and the strong diamagnetic component perpendicular to the molecular plane ($\sigma_{\perp}$). This behavior is well reproduced within the CROHF methods. Let us now turn to the visualization and discussion of the physical mechanisms underlying the results obtained for the EPR and NMR observables in terms of the maps of $\mathbf{J}^{(0)}$ (Figures 1−3), maps of $A^1{}_{\alpha}\beta(\mathbf{r})$ (Figure 4), and maps of $\mathbf{J}^{(1)}$ (Figures 5−7).

*6.1.1. Spin Currents and Density of Hyperfine Coupling Constant. BH₂.* The ROHF spin current density maps for the BH2 radical are shown in Figure 1. For an external magnetic

**Figure 2.** Streamlines (left column) and modulus (right column) of the ROHF spin-current density $\mathbf{J}^{(0)}$ characterizing the magnetic field-split ground-state doublet of $CH_2^-$, plotted for three different orientations of the field (quantization axis): (a) and (b) field along the $C_2$ axis; (c) and (d) field in the molecular plane and perpendicular to the $C_2$ axis; and (e) and (f) field perpendicular to the molecular plane. All maps are plotted over a plane containing the carbon atom.



**Figure 3.** Streamlines (left column) and modulus (right column) of the ROHF spin-current density $\mathbf{J}^{(0)}$ characterizing the magnetic field-split ground-state doublet of $NH_2$, plotted for three different orientations of the field (quantization axis): (a) and (b) field along the $C_2$ axis; (c) and (d) field in the molecular plane and perpendicular to the $C_2$ axis; and (e) and (f) field perpendicular to the molecular plane. All maps are plotted over a plane containing the nitrogen atom.

field oriented along the $C_2$ symmetry axis, the current density plotted in the perpendicular plane at the height of the boron atom (Figure 1a) consists of three paramagnetic (anticlockwise) vortices: one centered on the boron atom and characterized by a peak of very large magnitude (see high positive peak in Figure 1b) and two other vortices, which are very weak in magnitude, and are displaced symmetrically at the sides of the central atom. When the current is plotted at different heights further away from B (not shown), the current density map appears very similar to that plotted in Figure 1a, although only the central vortex survives with significant intensity. For the two orientations of the field perpendicular to the $C_2$ axis, the corresponding maps of spin current density display a pattern that resembles a distorted p atomic orbital, carrying two paramagnetic vortices (Figure 1c,e) of similar intensity (Figure 1d,f) centered on its lobes. The circulation on one of the two lobes is centered on the
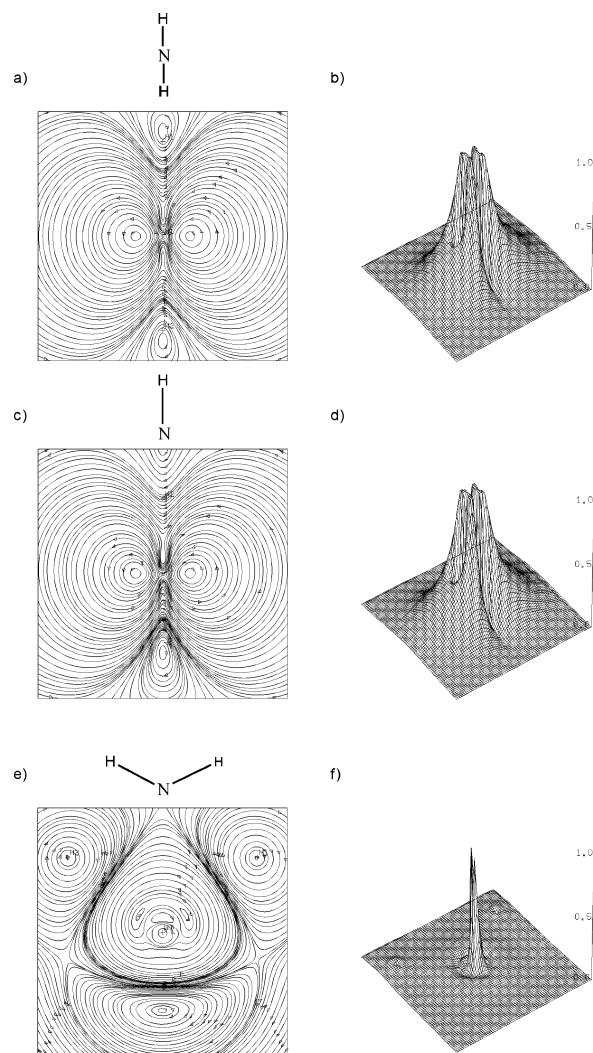
boron atom. For both orientations perpendicular to the $C_2$ axis, at different heights further away from B (not shown here), the current density maps are similar in appearance to those reported in Figure 1c,e, although the modulus of the paramagnetic vortex centered on B quickly becomes very small in magnitude, so that the dominant feature is represented by a localized paramagnetic circulation centered on the lobe that does not enclose the boron atom.

The maps can be readily understood in terms of the valence electronic structure of BH2. This can be described on the basis of three $sp^2$ hybrid atomic orbitals (AOs) contained in the molecular plane. With respect to a plane containing the $C_2$ axis and perpendicular to the molecular plane, two of the three $sp^2$ hybrids form two doubly occupied MOs in combination with the hydrogen s AO, one symmetric ($a_1$) and one antisymmetric ($b_2$). The third $sp^2$ hybrid ($a_1$) lies along the $C_2$ axis and hosts the unpaired electron density,

Charge and Spin Currents in Open-Shell Molecules
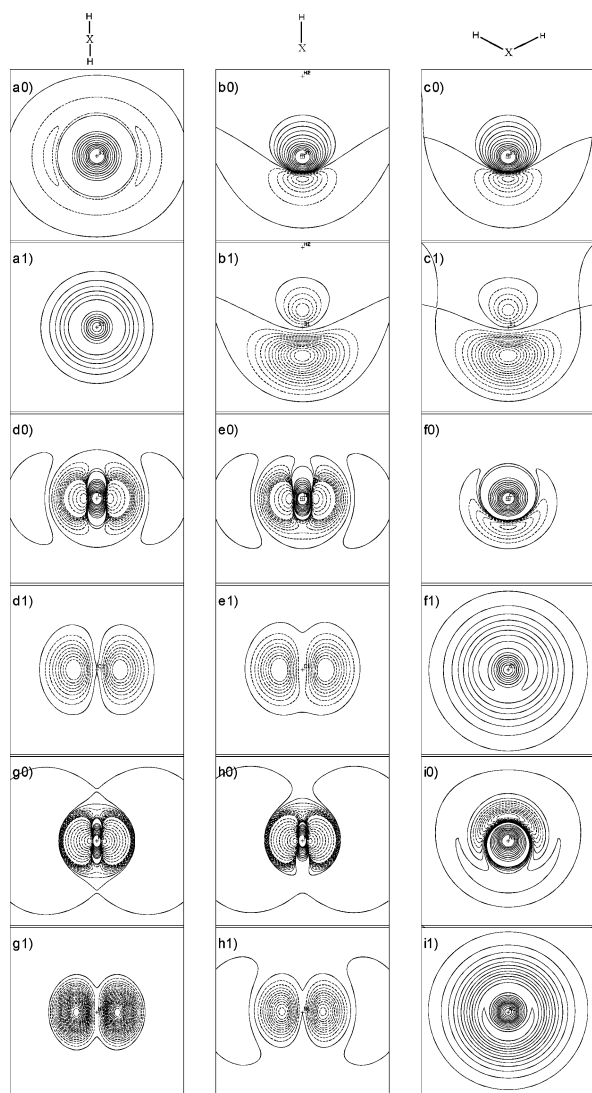
*J. Chem. Theory Comput., Vol. 3, No. 6, 2007* **2251**



**Figure 4.** Contour maps of nuclear hyperfine coupling density $A^X_{\alpha\beta}(\mathbf{r})$ (X = B, C, N) for the three radicals $BH_2$ (first two rows, a0, a1, b0, b1, c0, c1) $CH_2^-$ (third and fourth rows, d0, d1, e0, e1, f0, f1), and $NH_2$ (last two rows, g0, g1, h0, h1, i0, i1), corresponding to the total (isotropic plus dipolar terms) tensor components $A_{C2}$ (left column), $A_{\parallel}$ (central column), and $A_{\perp}$ (right column). Solid (dashed) lines correspond to positive (negative) density. Figures labeled x0 (x = a, b, c, d, e, f, g, h, i) correspond to planes containing the heavy nucleus, whereas the ones labeled x1 correspond to planes at 0.4 a0 from the heavy nucleus. The quantization axis corresponds to the $C_2$ axis (a−c); the axis perpendicular to $C_2$ and contained in the molecular plane (d−f); and the axis perpendicular to the molecular plane (g−i). The contour lines are plotted from −1 to 1 au, in steps of 0.1 au. For planes containing the heavy nuclei, 20 contour lines ± $e^r$ au were added, with $r$ ranging from 0.5 to 5.5 in steps of 0.5.

**Figure 5.** Streamlines (left column) and modulus (right column) of the CROHF-DZ first-order current density $\mathbf{J}^{(1)}$ induced in $BH_2$, by an external magnetic field plotted for three different orientations of the field: (a) and (b) field along the $C_2$ axis; (c) and (d) field in the molecular plane and perpendicular to the $C_2$ axis; and (e) and (f) field perpendicular to the molecular plane. All maps are plotted over a plane containing the boron atom.

i.e., it represents the singly occupied molecular orbital (SOMO). Seen along the $C_2$ axis and projected onto a perpendicular plane, the $a_1$ SOMO can be seen as an s atomic orbital hosting one unpaired electron. Accordingly, the corresponding spin current map shown in Figure 1a consists mainly of a single paramagnetic vortex centered on the B nucleus.
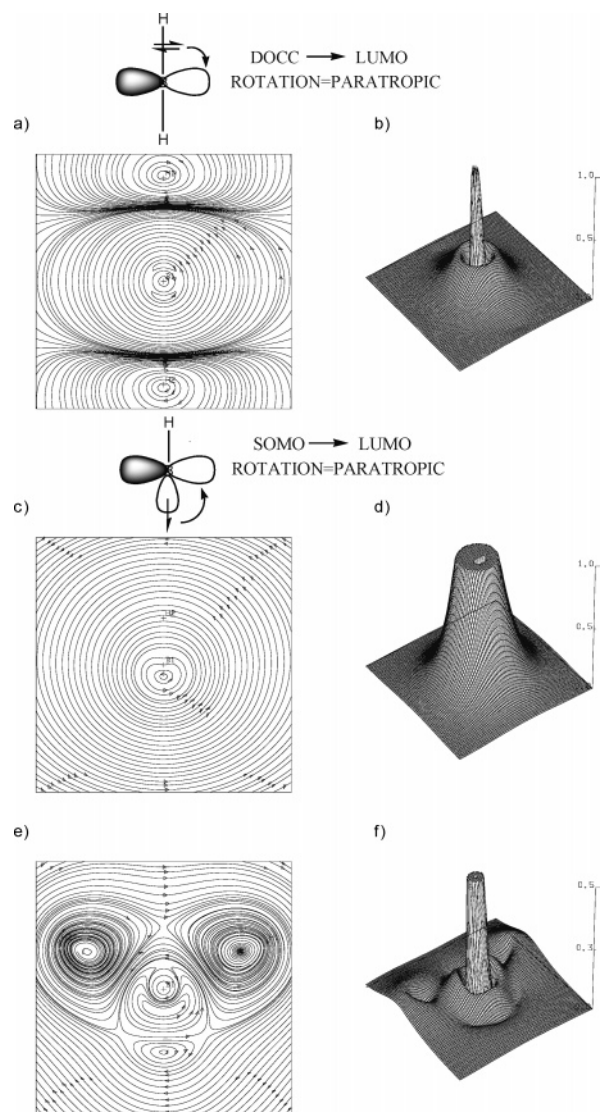
The corresponding map of HCC density $A_{\alpha\beta}(\mathbf{r})$ reported in Figure 4a0 provides a clear picture of the contribution of $\mathbf{J}^{(0)}$ to the integrated HCC tensor components. As detailed in ref 35, magnetic property density functions provide a map of the contribution to the magnetic field calculated at a given point in space (e.g., at the B site in this case) arising from current density patterns distributed all over the molecular domain. The contribution to the integrated HCC arising from a given current density pattern is ruled by the Biot-Savart law of classical electrodynamics. In particular, such a contribution is positive (negative) if the field induced at the probe site is reinforcing (opposing) the external magnetic field. At the height of the B atom, the current is dominated by the isotropic Fermi contact contribution to the HCC (see eq 8). This contribution is represented by the large peak of positive HCC density in Figure 4a0, which indicates that
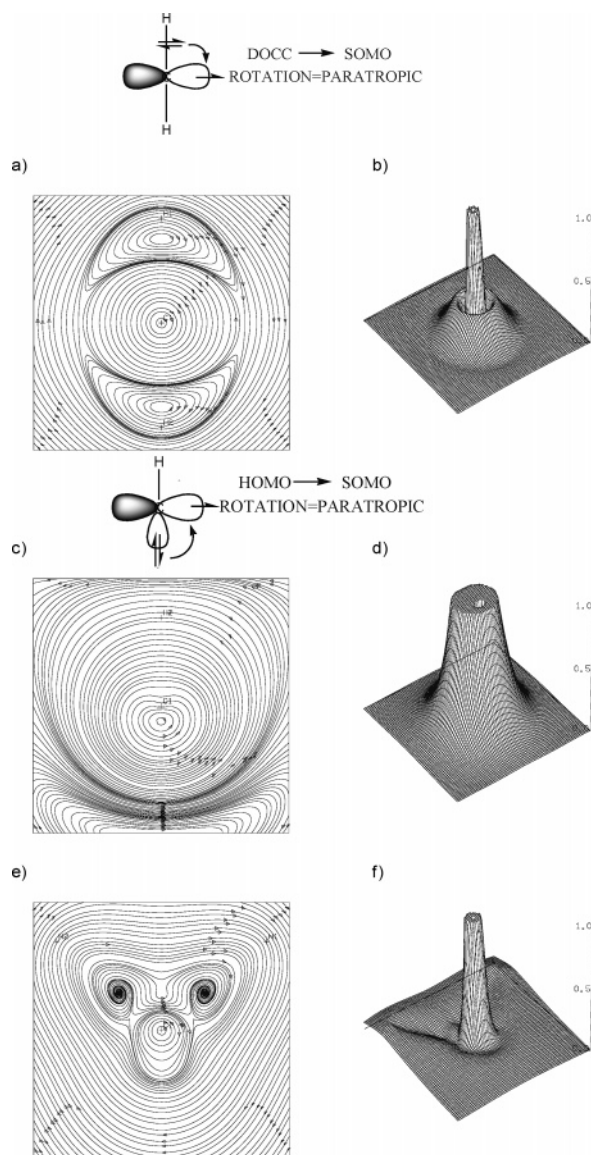
**Figure 6.** Streamlines (left column) and modulus (right column) of the CROHF-DZ first-order current density $\mathbf{J}^{(1)}$ induced in $CH_2^-$ by an external magnetic field, plotted for three different orientations of the field: (a) and (b) field along the $C_2$ axis; (c) and (d) field in the molecular plane and perpendicular to the $C_2$ axis; and (e) and (f) field perpendicular to the molecular plane. All maps are plotted over a plane containing the carbon atom.

**Figure 7.** Streamlines (left column) and modulus (right column) of the CROHF-DZ first-order current density $\mathbf{J}^{(1)}$ induced in $NH_2$, by an external magnetic field, plotted for three different orientations of the field: (a) and (b) field along the $C_2$ axis; (c) and (d) field in the molecular plane and perpendicular to the $C_2$ axis; and (e) and (f) field perpendicular to the molecular plane. All maps are plotted over a plane containing the nitrogen atom.

the paramagnetic vortex centered on B produces a local magnetic field parallel to the external field. The fact that plots at different heights are characterized by similar current density maps can be clearly seen on the map of HCC density plotted at 0.4 $a_0$ distance from the plane containing B (Figure 4a1), from which it is evident that the boron atom is still fully enclosed within a shielding cone produced by the dominant paramagnetic vortex. This explains the positive sign of $A_{C2}$ for boron.

The situation is rather different for the other two orientations of the quantization axis (Figure 1c,e). In these two cases the unpaired electron density is polarized along directions perpendicular to the SOMO axis. The associated spin current consists of two paratropic circulations centered on the two
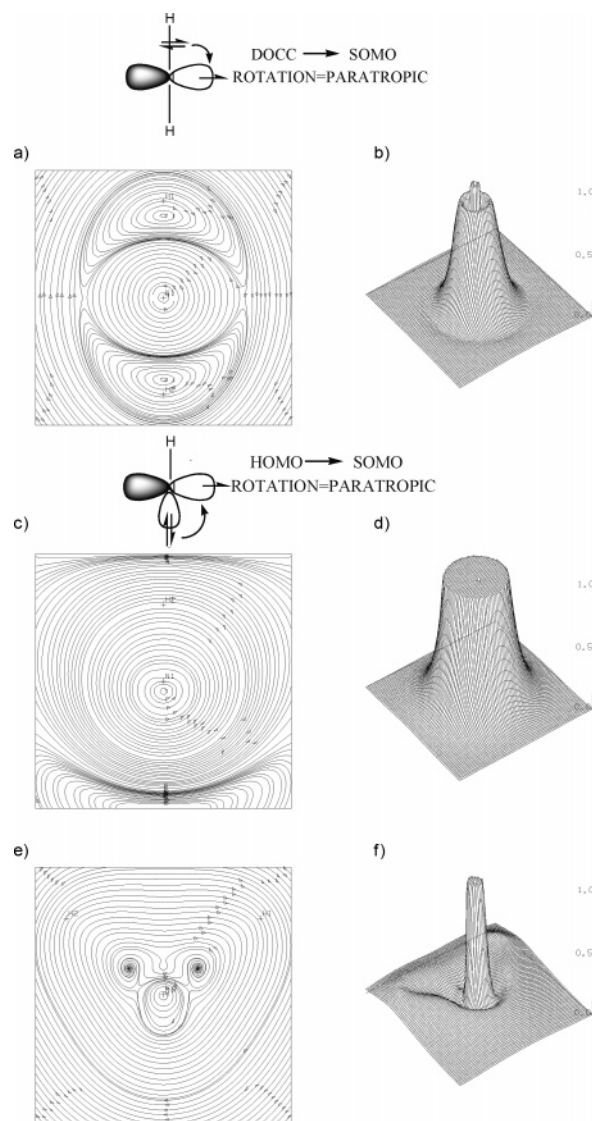
lobes of the $sp^2$ hybrid SOMO. One of the two paramagnetic vortices is centered on B, producing a local field parallel to the external one, thus providing a positive contribution to the integrated HCC (see the high positive peak centered on B in the maps of hyperfine coupling density, Figure 4b0,4c0). On the other hand, the paratropic circulation centered on the lobe of the $sp^2$ hybrid that does not enclose the boron atom provides a net negative contribution to the integrated HCC (see the negative peak in Figure 4b0,4c0). This fact can easily be understood in terms of the Biot-Savart law. The boron atom lies outside the shielding cone characterizing the Biot-Savart magnetic field distribution induced by the neighboring paramagnetic circulation, and, accordingly, it experiences an induced field that opposes the external one. In the plane containing the boron atom the positive contact contribution

prevails, leading to a positive $A_{iso}$. However, at heights further away from the plane containing B, the paramagnetic circulation that does not enclose the nuclear probe becomes the dominant feature (see Figure 4b1,4c1), a fact that rationalizes the negative values of $A_{\parallel}$ and $A_{\perp}$ reported in Table 1.

*$CH_2^-$ and $NH_2$.* The radicals $CH_2^-$ and $NH_2$ share almost identical spin current density maps (see Figures 2 and 3). This fact is a consequence of their virtually identical valence electronic structure. In particular, in both cases the valence space can be described on the basis of three $sp^2$ hybrid atomic orbitals (AOs) centered on the heavy nucleus and confined to the molecular plane and one p AO perpendicular to the molecular plane. The three MOs formed by the symmetric ($a_1$) and antisymmetric ($b_2$) combination of two $sp^2$ hybrid atomic orbitals, and the third $sp^2$ hybrid ($a_1$) pointing in the $C_2$ direction, are now all doubly occupied, the latter hosting a lone pair. In both radicals, the unpaired electron density occupies the perpendicular p AO ($b_1$), which thereby now represents the SOMO. When the external field is chosen along the $C_2$ axis, or perpendicular to it but contained in the molecular plane, the electron spin density distribution is polarized along directions perpendicular to the axis of the p SOMO. Accordingly, the associated spin current density plotted on planes perpendicular to the field displays the typical shape of a p orbital (see Figures 2a,c and 3a,c). In particular, the spin current density map consists of two paramagnetic circulations localized on the lobes of the p AO. Because of the spin polarization effects approximately described by the UHF wave function, also the s orbital on the heavy nucleus carries a nonzero spin density. This translates into a spin current connecting the two lobes, which is equivalent to an effective paramagnetic vortex centered on the heavy nucleus, associated with a Fermi contact contribution to $\mathbf{J}^{(0)}$.

At the height of the heavy nuclei, the Fermi contact circulation dominates the current density maps and results in a positive isotropic HCC. The signature of the contact current can be observed on the maps of $A_{\alpha\beta}(\mathbf{r})$ as a positive peak centered on the heavy nucleus (see Figure 4d0,e0,g0,h0). Further away from the plane containing the heavy nuclei, the two paramagnetic lobe-centered circulations become the dominant feature in the maps, and, since the central nucleus lies outside their anisotropy shielding cones, it experiences an induced field that opposes the external one, resulting in a negative contribution to the integrated HCC. This can be clearly seen in the maps of HCC density in terms of two steep negative peaks centered at the sides of the heavy atom, both at the height of the C and N nuclei (see Figure 4d0,e0,g0,h0), and, even more clearly, at 0.4 $a_0$ above (Figure 4d1,e1,g1,h1). The deshielding effect arising from the two paramagnetic circulations that do not enclose the nuclear probe rationalizes the negative signs of $A_{C2}$ and $A_{\parallel}$ reported in Table 1 for $CH_2^-$ and $NH_2$.

A magnetic field perpendicular to the molecular plane polarizes the spin density along the p SOMO axis. Accordingly, any plot on a plane perpendicular to this direction can be interpreted in terms of a projection of the unpaired electron density on an *s*-like orbital. The maps of spin current density reported in Figures 2e and 3e are indeed dominated by a

single paramagnetic vortex centered on the heavy nucleus, as shown by the corresponding maps of HCC density in Figure 4f0,f1,i0,i1. This results in the positive $A_{\perp}$ are reported in Table 1.

*6.1.2. First-Order Current Density and Temperature-Independent Contribution to Nuclear Magnetic Shielding.* $BH_2$. Figure 5 shows the maps of current density induced in the $BH_2$ radical by an external magnetic field, calculated at the CROHF-DZ level of theory. For a field oriented along the $C_2$ axis (Figure 5a), the induced current density distribution is dominated by two concentric counter-rotating circulations: diatropic (clockwise) and strong the inner one, weak and paratropic the outer one. The inner circulation represents the diamagnetic response of the core electrons. Within the minimal valence space, the outer paratropic circulation can be rationalized as follows. It has been shown that diatropic and paratropic contributions to the first-order current density in closed-shell molecules are associated with virtual transitions from occupied to unoccupied MOs.[24,25]

A given transition provides a diatropic (paratropic) contribution to the total current, if by symmetry it is electric (magnetic) dipole allowed, with respect to those components of the electric (magnetic) dipole operator perpendicular (parallel) to the magnetic field. The intensity of the contribution is proportional to the inverse of the energy gap between the two intervening MOs (which implies that frontier orbital contributions will dominate the response) and depends on the degree of overlap between the occupied MO and the virtual MO transformed by the relevant electric or magnetic dipole operator. The phenomenology of magnetically active orbital transitions in open-shell molecules is enriched by the possibility of nonzero matrix elements between doubly occupied and singly occupied MOs and between singly occupied and virtual MOs. A detailed analysis of all possibilities goes beyond the scope of the present work. Nevertheless, some elementary pictorial concepts based on these symmetry selection rules can help the rationalization of the present results.

When the field lies along the $C_2$ axis, the transition from the doubly occupied antisymmetric combination $b_2$ of in-plane $sp^2$ hybrid AOs to the lowest unoccupied molecular orbital (LUMO) $b_1$ is magnetic dipole allowed, i.e., it is rotationally allowed with respect to the $a_2$ rotation about an axis parallel to the field (see the scheme above Figure 5a), since $b_2 \times a_2 \times b_1 \supset a_1$. Hence, the observed paratropic circulation can be rationalized in terms of the $b_2$ to $b_1$ rotationally allowed transition. However, the energy gap between the doubly occupied $b_2$ and the LUMO $b_1$ can be quite large. Also, because of the nonlinear geometry of $BH_2$, only a fraction of the $b_2$ doubly occupied MO overlaps with the $b_1$ LUMO after the action of the perpendicular magnetic dipole operator, which explains the weak paratropic response shown in Figure 5a,b, and the small negative value for $\sigma_{C2}$ reported in Table 2.

A different situation is encountered for a field oriented perpendicular to the $C_2$ axis and contained in the molecular plane. As shown in Figure 5c, the induced current density map in this case is dominated by a strong paramagnetic vortex centered just below the B atom. This pattern can be

understood in terms of the rotationally allowed transition from the $a_1$ SOMO to the $b_1$ LUMO, as illustrated in the scheme above Figure 5c. The large magnitude of this transition (and of the corresponding induced current) is due both to the small energy gap between SOMO and LUMO and to the strong overlap between the $a_1$ sp$^2$ hybrid after the action of a rotation and the coplanar p LUMO. This transition and the resulting paratropic current explains the large and negative value for $\sigma_{||}$ reported in Table 2, which also dominates the isotropic response. Finally, it is easy to see that with respect to a rotation about an axis perpendicular to the molecular plane, within the frontier orbital space, there is no transition that is rotationally allowed. Accordingly, the response to a magnetic field oriented along this direction is described by a map of induced current density (Figure 5e,f) dominated by a diatropic circulation centered on the B nucleus, leading to a positive $\sigma_\perp$.

*CH$_2^-$ and NH$_2$.* The maps of $\mathbf{J}^{(1)}$ for CH$_2^-$ and NH$_2$ (Figures 6 and 7) present many features in common with those obtained for BH$_2$. In particular, also in this case the current density map for fields oriented along the $C_2$ axis (Figures 6a and 7a) or perpendicular to $C_2$ but contained in the molecular plane (Figures 6c and 7c), is characterized by a paratropic response, weak in the former case, and very strong in the latter. When the field lies along the $C_2$ axis, the current pattern can be described in terms of a strong, inner diatropic circulation centered on the heavy atom and an outer concentric counter-rotating partropic circulation. The paratropicity originates from a transition from the doubly occupied $b_2$ MO, to the $b_1$ p SOMO. The fact that this transition appears to dominate the response in BH$_2$ and NH$_2$ leading to a negative $\sigma_{C2}$ but is overwhelmed by the core diatropic response in CH$_2^-$, leading to a positive $\sigma_{C2}$, can be qualitatively rationalized on the basis of pure geometrical arguments. The experimental geometries employed in the present calculations are characterized by H$-$X$-$H angles of 131° (X = B), 103° (X = N), and 99.7° (X = C). Clearly, the smaller the HXH angle (CH$_2^-$ is characterized by the smallest value), the smaller the component of the antisymmetric combination of sp$^2$ hybrids ($b_2$ HOMO) that overlaps with the $b_1$ p-SOMO (or LUMO in the case of BH$_2$) when rotated by the relevant magnetic dipole operator, and, accordingly, the smaller the contribution of the paratropic transition to the total induced current.

A magnetic field perpendicular to the $C_2$ axis and contained in the molecular plane induces a strong paratropic current density vortex, as in the BH$_2$ case (see Figures 6c,d and 7c,d). The rotationally allowed transition at the heart of the observed paratropicity occurs between the $a_1$ HOMO (the lone pair) and the p-like $b_1$ SOMO, as for the BH$_2$ radical, although in that case the transition occurred between the SOMO and the LUMO. The resulting $\sigma_{||}$, large and negative, is a clear consequence of the overwhelming paratropic circulation. Once again, since no transition within the frontier orbital space is rotationally allowed, the response to a magnetic field along the direction perpendicular to the molecular plane is dominated by a diatropic circulation centered on the heavy nucleus, which leads to positive and large $\sigma_\perp$ (see Table 2).

**Scheme 1**
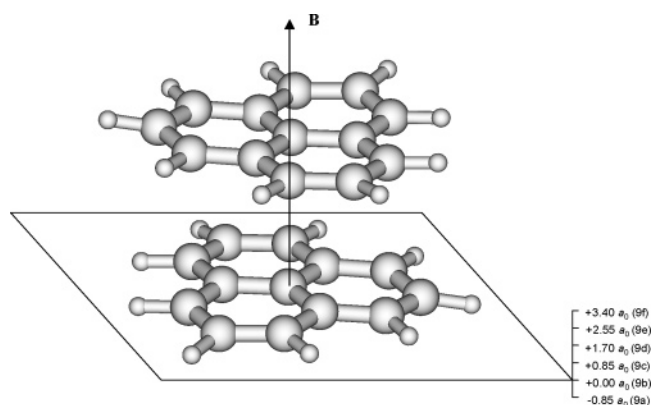


6.2. **Current Density Maps for the Pancake-Bonded Dimer of the Neutral Phenalenyl Radical.** The NMR spectrum of the (open-shell singlet) pancake-bonded dimer of the neutral phenalenyl radical has been recently reported[37] and interpreted in terms of the existence of global diatropic ring currents, whose signature in the NMR spectrum is represented by the downfield chemical shift (6.47 ppm) assigned to the proton directly bonded to the aromatic phenalenyl rings (for a model system see Scheme 1). The model on which the assignment relies, i.e., the ring current model, would thus classify the $\pi$-dimeric complex as an aromatic molecule, according to the magnetic criterion,[19-22] a fact that was used to corroborate the evidence for the chemical stability of the experimentally characterized complex.[37] The ring current model was further tested and confirmed in ref 37 from a computational standpoint by means of NICS calculations.[21] However, there exists some dispute in the literature as to whether isotropic averages such as downfield proton chemical shifts and NICS calculations can in fact be always considered as reliable magnetic aromaticity indicators,[50,51] especially when the focus is on polycyclic systems as in the present case. Hence, direct visualization of $\mathbf{J}^{(1)}$ in order to test the existence of a ring current in this open-shell singlet represents an important piece of information to assess the magnetic aromaticity of this molecule and represents a natural application of the newly developed methodology. To ensure the open-shell singlet character of the phenalenyl dimer we employed a UDFT method with the GGA functional HCTH,[31] available in Gaussian 03,[44] which has been shown to improve on the calculation of magnetic properties over conventional GGA functionals. From the unperturbed KS orbitals obtained from a Gaussian 03 calculation with a cc-pVDZ basis set, we computed $\mathbf{J}^{(1)}$ using the newly implemented routines in the SYSMO package.[42]

Note that, due to the broken symmetry nature of the solutions obtained from the unrestricted DFT method, an unphysical spin current density $\mathbf{J}^{(0)}$ is obtained for the $\pi$-dimeric complex of the phenalenyl radical, despite the fact that its ground state should be a singlet. This is clearly a drawback of the chosen approach. However, two reasons can justify its use in the present investigation. First, the shielding and NICS calculations reported in ref 37 have been performed within the same general approach, i.e., they are broken symmetry DFT calculations, so that the visual
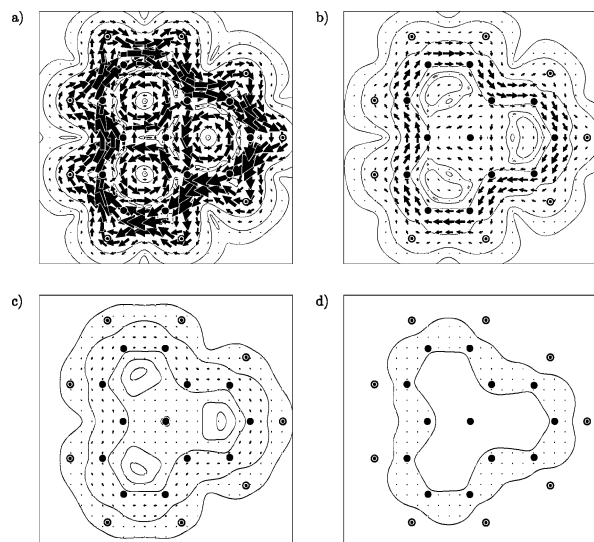
Charge and Spin Currents in Open-Shell Molecules

*J. Chem. Theory Comput.*, Vol. 3, No. 6, 2007 **2255**



**Figure 8.** Maps of unrestricted HCTH-(GGA)DFT current density $J^{(1)}$ induced in $D_{3h}$ neutral phenalenyl radical by a magnetic field perpendicular to the molecular plane plotted as arrows whose area is proportional to the current modulus. The maps show plots on a plane parallel to the molecular plane and distant from it: (a) 0.85 $a_0$ ($j_{max} = 0.0929$ $c$ au), (b) 1.7$a_0$ ($j_{max} = 0.0332$ $c$ au), (c) 2.55 $a_0$ ($j_{max} = 0.0073$ $c$ au), and (d) 3.4 $a_0$ ($j_{max} = 0.0018$ $c$ au). Black filled circles (dotted circles) correspond to carbon (hydrogen) nuclei. (Anti)clockwise circulations correspond to diatropic (paratropic) currents.

analysis proposed here is fully consistent with the results that are the object of this analysis. Second, given that spin−orbit coupling can be neglected for this system, we can reasonably expect that the maps of $J^{(1)}$ obtained from the present broken symmetry calculations will survive at least qualitatively unchanged to more accurate treatments.

First, we computed $J^{(1)}$ for the neutral phenalenyl monomer. This organic radical is an odd-alternant hydrocarbon with high symmetry ($D_{3h}$) and is stable in solution under an inert gas atmosphere.[52] The molecule has the ability to form three redox species: cation, radical, and anion. Whereas the ring current aromaticity of the closed shell anion and cation has been assessed via ab initio calculations,[53] no such investigation has been undertaken to date on the ring-current response of the neutral radical system. Accordingly, we first proceeded with the optimization of its $D_{3h}$ structure at the UB3LYP/6-31G* level of theory using the program Gaussian 03.[44] Then we computed the UHCTH/cc-pVDZ maps of current density induced by a magnetic field perpendicular to the molecular plane, over two-dimensional regular grids defined on planes parallel to the molecular plane, up to 3.4 $a_0$ distance from it (about half the separation between the two phenalenyl units in the pancake-bonded dimer). In Figure 8 the resulting maps of $J^{(1)}$ are reported: it is evident that the dominant motif can be described in terms of a large diatropic ring current circulating over the 12-carbon perimeter, a clear-cut signature of the magnetic aromaticity of this neutral radical system. At 0.85 $a_0$ (Figure 8a), close to the maximum of $\pi$-electron density, we can observe the ring current at its maximal strength ($j_{max} = 0.0929$ $c$ au). Further away from the molecular plane the $\pi$-electron ring current



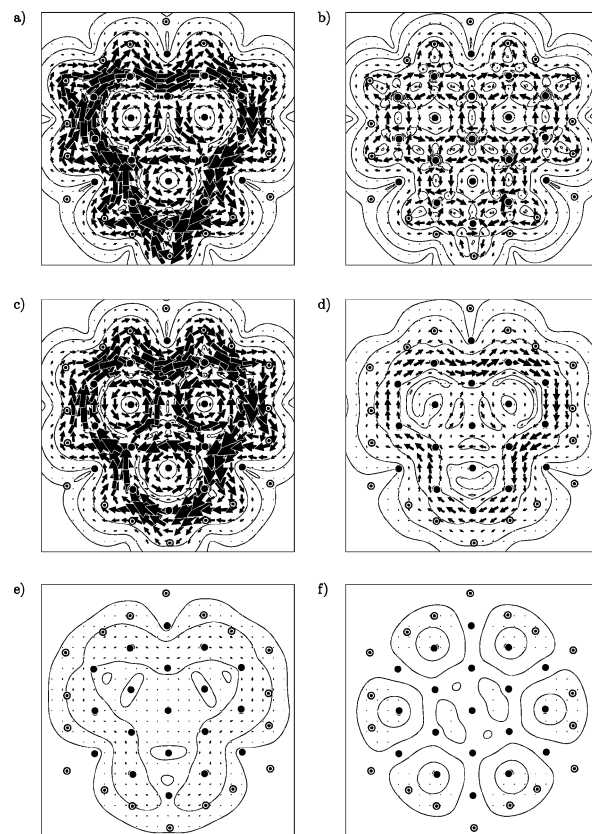**Figure 9.** Maps of unrestricted HCTH-GGA-DFT current density $J^{(1)}$ induced in the pancake-bonded dimer of the neutral phenalenyl radical by a magnetic field (**B**) oriented along the direction connecting the two carbon nuclei at the center of the two monomers (see Scheme 1). The maps show projections of $J^{(1)}$ on planes at (a) $-0.85$ $a_0$ ($j_{max} = 0.1065$ $c$ au), (b) 0.0 $a_0$ ($j_{max} = 1.957$ $c$ au), (c) $+0.85$ $a_0$ ($j_{max} = 0.1054$ $c$ au), (d) $+1.7$ $a_0$ ($j_{max} = 0.0433$ $c$ au), (e) $+2.55$ $a_0$, ($j_{max} = 0.0093$ $c$ au), and (f) $+3.4$ $a_0$ ($j_{max} = 0.0063$ $c$ au) distance from the average height along **B** of the carbon nuclei belonging to one of the nearly planar monomers (see Scheme 1). A scaling (reduction) factor of about 0.3 has been applied to the plot on the molecular plane (b) to ease the visualization.

is still visible (Figure 8b,c), although progressively dying off, so that at 3.4 $a_0$ (Figure 8d) hardly anything is still visible, the maximal modulus of the current density being only about $j_{max} = 0.0018$ $c$ au.

Next we performed the current density response calculations within the broken symmetry approximation for the pancake-bonded dimer cast in the $C_i$ geometry optimized at the UB3LYP/6-31G* reported in ref 37, but here the *tert*-butyl groups were replaced by hydrogen nuclei and the six new H−C distances reoptimized keeping all other degrees of freedom frozen at the same level of theory. In Figure 9 we report the maps of $J^{(1)}$ induced in the dimeric $\pi$-complex by a magnetic field **B** oriented along the direction connecting the two carbon atoms at the center of the two phenalenyl monomers (chosen as the $z$-axis) and plotted on planes perpendicular to **B**. The current density plotted on planes at $\pm 0.85$ $a_0$ distance from the average height along **B** of the carbon nuclei belonging the nearly planar bottom-monomer (see Scheme 1) consists of a strong global diatropic ring

current, almost undistinguishable from that plotted at the corresponding height for the $D_{3h}$ monomer, although slightly stronger in magnitude in the dimer case ($j_{max}$(dimer) $\approx 0.106$ c au, $j_{max}$(monomer) $\approx 0.093$ $c$ au). Moving toward the middle region of the pancake-bonded dimer, we can observe that the current dies off basically as quickly as in the monomer case (compare Figure 8b–d with Figure 9d–f) although the maximal current magnitude remains consistently larger in the dimer case (see $j_{max}$ values in the captions to Figures 8 and 9). The slightly larger magnitude of the $\mathbf{J}^{(1)}$ modulus for the dimer in the region of space bracketed by the two monomeric units when compared with that at corresponding heights for the phenalenyl radical can be rationalized in terms of the additional electron density shifted in such region as a consequence of the formation of a weak pancake bond (see ref 37 for a detailed discussion). The increased electron density with respect to the monomer case gives rise to a larger diamagnetic contribution to the ring current.

However, it is interesting to note that the large aromatic NICS values computed in the region between the two monomers are clearly due both to the concerted action of the two bracketing ring currents, which are evidently "localized" above and below such region, and to the slight increase in electron density (and consequently in diatropic current density) in the region between the two monomers, but *no significant ring current exists in the pancake-bond region*. The stronger monomeric ring currents and the electron density shift lead on integration to NICS values that have been shown in ref 37 to be larger in magnitude than the value one would obtain by adding up the distinct contributions from each single monomer. The maps in Figure 9 clearly show that the NICS enhancement is indeed a signature of the aromatic character of the $\pi$-complex but also show as clearly that this is mostly due to an overall enhancement of the local aromaticity of the two monomers (which, in fact, are magnetically aromatic in their own right, as seen from Figure 8) rather than to the existence of a significant ring current in the pancake-bonding region. In this respect it appears evident how the actual plot of $\mathbf{J}^{(1)}$ in addition to recovering the information provided by the NICS scan reported in ref 37 leads to a richer picture of the actual space-distribution of the aromatic regions of the molecule, a kind of information that gets completely lost upon integration.

## 7. Conclusions

In this work we developed a consistent theoretical and computational approach to the representation of the magnetic response of open-shell molecules with small spin–orbit coupling in terms of ab initio spin and charge current density vector fields. Preliminary investigations show that the newly introduced methodology provides a powerful tool for the interpretation of the mechanisms underlying the observables measured in the NMR and ESR experiments, in terms of simple concepts from classical electrodynamics and basic molecular orbital theory.

**Supporting Information Available:** Cartesian coordinates of the 5 molecules for which the calculations presented in the present work have been performed. This material is available free of charge via the Internet at http://pubs.acs.org.

### References

(1) Mile, B. *Curr. Org. Chem.* **2000**, *4*, 55−83.

(2) Stubbe, J.; van der Donk, W. *Chem. Rev.* **1998**, *98*, 705−762.

(3) Turro, N. J.; Kleinman, M. H.; Karatekin, E. *Angew. Chem., Int. Ed.* **2000**, *39*, 4436−4461.

(4) Bertini, I.; Luchinat, C.; Parigi, G.; Pierattelli, R. *ChemBioChem* **2005**, *6*, 1536−1549.

(5) McConnell, H. M.; Chesnut, D. B. *J. Chem. Phys.* **1958**, *28*, 107−117.;

(6) Atherton, N. M. *Principles of Electron Spin Resonance*; Ellis Horwood and PTR Prentice Hall Press: New York, 1993.

(7) Lushington, G. H.; Grein, F. *Theor. Chim. Acta* **1996**, *93*, 259−267.

(8) Jayatilaka, D. *J. Chem. Phys.* **1998**, *108*, 7587−7594.

(9) Neese, F. *J. Chem. Phys.* **2001**, *115*, 11080−11096.

(10) Improta, R.; Barone, V. *Chem. Rev.* **2004**, *104*, 1231−1253.

(11) Rinkevicius, Z.; Vaara, J.; Telyatnyk, L.; Vahtras, O. *J. Chem. Phys.* **2003**, *118*, 2550−2561.

(12) Moon, S.; Patchkovskii, S. In *Calculation of NMR and EPR parameters*; Kaupp, M., Bühl, M., Malkin, V. G., Eds.; Wiley: Weinheim, 2004; Part B, Chapter 20, pp 325−338.

(13) Pennanen, T. O.; Vaara, J. *J. Chem. Phys.* **2005**, *123*, 174102.

(14) Hrobàrik, P.; Reviakine, R.; Arbuznikov, A.; Malkina, O. L.; Malkin, V. G.; Köhler, F. H.; Kaupp, M. *J. Chem. Phys.* **2007**, *126*, 024107.

(15) London, F. *J. Phys. Radium* **1937**, *8*, 397−409.

(16) Pauling, L. *J. Chem. Phys.* **1936**, *4*, 673−677.

(17) Pople, J. A. *J. Chem. Phys.* **1956**, *24*, 1111.

(18) Lazzeretti, P. *Prog. Nucl. Magn. Reson. Spectrosc.* **2000**, *36*, 1−88.

(19) Elvidge, J. A.; Jackman, L. M. *J. Chem. Soc.* **1961**, 859−866.

(20) Dauben, H. J.; Wilson, J. D.; Laity, J. L. *Nonbenzenoid aromatics;* Snijder, J. P., Ed.; Academic Press: New York, 1971; Vol. II.

(21) Schleyer, P. v. R.; Maerker, C.; Dransfeld, A.; Jiao, H.; van Eikema, Hommes, N. J. R. *J. Am. Chem. Soc.* **1996**, *118*, 6317−6318.

(22) Fowler, P. W.; Steiner, E.; Havenith, R. W. A.; Jenneskens, L. W. *Magn. Reson. Chem.* **2004**, *42*, S68−S78.

(23) Fowler, P. W.; Steiner, E.; Jenneskens, L. W. *Chem. Phys. Lett.* **2003**, *371*, 719−723.

(24) Steiner, E.; Fowler, P. W. *Chem. Commun. (Cambridge)* **2001**, 2220−2221.

(25) Steiner, E.; Fowler, P. W. *J. Phys. Chem. A* **2001**, *105*, 9553−9562.

Charge and Spin Currents in Open-Shell Molecules

*J. Chem. Theory Comput., Vol. 3, No. 6, 2007* **2257**

(26) Abragam, A.; Bleaney, B. *Electronic Paramagnetic Resonance of Transition Ions*; Oxford University Press: London, 1970.

(27) McWeeny, R. *Methods of Molecular Quantum Mechanics*; Academic Press: London, 1989.

(28) Pickard, C. J.; Mauri, F. *Phys. Rev. Lett*. **2002**, *88*, 086403.

(29) Patchkovskii, S.; Schreckenbach, G. In *Calculation of NMR and EPR parameters*; Kaupp, M., Bühl, M., Malkin, V. G., Eds.; Wiley: Weinheim, 2004; Part D, Chapter 32, pp 505−530.

(30) Patchkovskii, S.; Strong, R. T.; Pickard, C. J.; Un, S. *J. Chem. Phys*. **2005**, *122*, 214101.

(31) Hamprecht, F. A.; Cohen, A. J.; Tozer, D. J.; Handy, N. C. *J. Chem. Phys*. **1998**, *109*, 6264−6278.

(32) Keal, T. W.; Tozer, D. J. *J. Chem. Phys*. **2003**, *119*, 3015−3023.

(33) Jameson, C. J.; Buckingham, A. D. *J. Phys. Chem*. **1979**, *83*, 3366.

(34) Soncini, A.; Lazzeretti, P. *J. Chem. Phys*. **2003**, *118*, 7165−7173.

(35) Soncini, A.; Fowler, P. W.; Lazzeretti, P.; Zanasi, R. *Chem. Phys. Lett*. **2005**, *401*, 164−169.

(36) Soncini, A.; Lazzeretti, P. *ChemPhysChem*. **2006**, *7*, 679−684.

(37) Suzuki, S.; Morita, Y.; Fukui, K.; Sato, K.; Shiomi, D.; Takui, T.; Nakasuji, K. *J. Am. Chem. Soc*. **2006**, *128*, 2530−2531.

(38) Landau, L. D.; Lifshitz, E. M. *Quantum Mechanics*; Pergamon: Oxford, 1981.

(39) Lazzeretti, P.; Malagoli, M.; Zanasi, R. *J. Mol. Struct. THEOCHEM* **1994**, *313*, 299−312.

(40) McWeeny, R.; Steiner, E. *Adv. Quantum Chem*. **1965**, *2*, 93−117.

(41) Juselius, J.; Sundholm, D.; Gauss, J. *J. Chem. Phys*. **2004**, *121*, 3952−3963.

(42) Lazzeretti, P.; Zanasi, R. *SYSMO package*; University of Modena: 1980. Additional routines for the evaluation and plotting of current density: E. Steiner, P. W. Fowler, R. W. A. Havenith, A. Soncini. For (C)ROHF, (C)UHF, and (U)GGA-DFT calculations: A. Soncini.

(43) McWeeny, R.; Diercksen, G. *J. Chem. Phys*. **1968**, *49*, 4852−4856.

(44) Frisch, M. J.; Trucks, G. W.; Schlegel, H. B.; Scuseria, G. E.; Robb, M. A.; Cheeseman, J. R.; Montgomery, J. A., Jr.; Vreven, T.; Kudin, K. N.; Burant, J. C.; Millam, J. M.; Iyengar, S. S.; Tomasi, J.; Barone, V.; Mennucci, B.; Cossi, M.; Scalmani, G.; Rega, N.; Petersson, G. A.; Nakatsuji, H.; Hada, M.; Ehara, M.; Toyota, K.; Fukuda, R.; Hasegawa, J.; Ishida, M.; Nakajima, T.; Honda, Y.; Kitao, O.; Nakai, H.; Klene, M.; Li, X.; Knox, J. E.; Hratchian, H. P.; Cross, J. B.; Bakken, V.; Adamo, C.; Jaramillo, J.; Gomperts, R.; Stratmann, R. E.; Yazyev, O.; Austin, A. J.; Cammi, R.; Pomelli, C.; Ochterski, J. W.; Ayala, P. Y.; Morokuma, K.; Voth, G. A.; Salvador, P.; Dannenberg, J. J.; Zakrzewski, V. G.; Dapprich, S.; Daniels, A. D.; Strain, M. C.; Farkas, O.; Malick, D. K.; Rabuck, A. D.; Raghavachari, K.; Foresman, J. B.; Ortiz, J. V.; Cui, Q.; Baboul, A. G.; Clifford, S.; Cioslowski, J.; Stefanov, B. B.; Liu, G.; Liashenko, A.; Piskorz, P.; Komaromi, I.; Martin, R. L.; Fox, D. J.; Keith, T.; Al-Laham, M. A.; Peng, C. Y.; Nanayakkara, A.; Challacombe, M.; Gill, P. M. W.; Johnson, B.; Chen, W.; Wong, M. W.; Gonzalez, C.; Pople, J. A. *Gaussian 03, Revision C.02*; Gaussian, Inc.: Wallingford, CT, 2004.

(45) Keith, T. A.; Bader, R. F. W. *Chem. Phys. Lett.* **1993**, *210*, 223−231.

(46) Lazzeretti, P.; Malagoli, M.; Zanasi, R. *Chem. Phys. Lett.* **1994**, *200*, 299−304.

(47) Zanasi, R. *J. Chem. Phys*. **1996**, *105*, 1460−1469.

(48) Baird, N. C. *J. Am. Chem. Soc*. **1972**, *94*, 4941−4948.

(49) Gogonea, V.; Schleyer, P. V. R.; Schreiner, P. R. *Angew. Chem., Int. Ed.* **1998**, *37*, 1945−1948.

(50) Wannere, C. S.; Corminboeuf, C.; Allen, W. D.; Schaefer, H. F., III; Schleyer, P. v. R. *Org. Lett.* **2005**, *7*, 1457 -1460.

(51) Faglioni, F.; Ligabue, A.; Pelloni, S.; Soncini, A.; Viglione, R. G.; Ferraro, M. B.; Zanasi, R.; Lazzeretti, P. *Org. Lett.* **2005**, *7*, 3457 -3460.

(52) Reid, D. H. *Q. Rev.* **1965**, *19*, 274.

(53) Cyranski, M. K.; Havenith, R. W. A.; Dobrowolski, M. A.; Gray, B. R.; Krygowski, T. M.; Fowler, P. W.; Jenneskens, L. W. *Chem. Eur. J.* **2007**, *13*, 2201−2207.